GPO PRICE $ _____

CFSTI PRICE(S) $ _____

X-611-66-112

Hard copy (HC) 2.00

Microfiche (MF) .50

NASA TM X- 55511

ff 653 July 65

ELECTRONS IN THE VAN ALLEN ZONE MEASURED WITH A SCINTILLATOR ON EXPLORER XIV

BY

G. PIZZELLA

L. R. DAVIS

J. M. WILLIAMSON

MARCH 1966

NASA

GODDARD SPACE FLIGHT CENTER

GREENBELT, MARYLAND

ELECTRONS IN THE VAN ALLEN ZONE MEASURED WITH A SCINTILLATOR ON EXPLORER XIV

G. Pizzella, L. R. Davis, and J. M. Williamson
Goddard Space Flight Center
Greenbelt, Maryland

Abstract

30334

The energy spectrum of electrons in the energy range from 5 to 160 kev is investigated near the equator, at L shells between 2 and 10, by using scintillator measurements on Explorer XIV. We find:

1. Peak values of 8×10^8 electrons/cm^2/sec with an average energy of ~50 kev at L ~ 5.
2. Peak values of 1.6×10^9 electrons/cm^2/sec with an average energy of ~ 10 kev at L $\gtrsim$ 8.
3. Time variations of intensity by factors of 10 or less above L ~ 4 during the 15 days of data under study.
4. A discontinuity of the energy spectrum at L ~ 7, with a general tendency for the spectrum to become softer at higher L.

The 10-kev electrons measured at L ~8 are trapped in the earth's magnetic field and appear not to be a tail of the outer belt electrons. These electrons are unable, without an accompanying replenishing mechanism, to supply the auroral regions.

Author

INTRODUCTION

Using a scintillator on Explorer XIV, we measured electrons of 5 to 160 kev trapped in the earth's magnetic field. This study is limited to a short period of time and therefore is not aimed at investigating temporal correlations. Space and angular distributions of electrons near the equatorial plane are shown for the eight orbits under study. The energy spectrum is studied with regard to space and pitch angle dependency. Equatorial omnidirectional intensities are computed from the experimental data for electrons with energy greater than 10 and 50 kev. The results are discussed and compared with the experimental results by Gringauz et al. [1960a, 1960b], Frank et al. [1963, 1964], and Freeman [1964].

EXPERIMENTAL APPARATUS

The satellite. A summary of the main orbital characteristics of Explorer XIV is given in Table I.

The satellite was supposed to be spin-stabilized. However, a small precession occurred soon after launch in October 1962. Later on, it increased up to an angle of 70° and again became small during January 1963. The precession makes the calculation of the pitch angle of the measured particles somewhat more complicated. As a first step toward a more complete analysis, we have limited this study to the period of time between October 5 and 16, 1962. During this period the total precession angle was 4° to 8° and has been ignored. Therefore, the error which arose in the pitch angle computation turned out to be

less than 4°, smaller than the acceptance angle of the detector.

Figure 1 gives the time and space (in McIlwain's coordinates) covered by this study. All the data considered here have local times between 8 and 10 a.m. (60° to 30° from the subsolar point).

The Detector. Details of the instrument are given by Davis and Williamson [1962]. Therefore, we shall just outline the operational principle and point out the features with which this research is concerned.

A collimator lets particles enter and hit a nickel absorber which is periodically changed by a step-moving wheel. Sixteen steps make it possible to measure background, electrons, protons, α-particles and to check the gain stability by means of two radioactive sources. For this study we have considered the steps of the moving wheel which are associated with a scatter geometry. In this geometry the particles with sufficient energy to pass through the absorber hit a gold surface; some of them are scattered into a ZnS (Ag) powdered phosphor scintillator which is on the face of a photomultiplier tube (Figure 2). The logarithm of the dc current from the 8th dynode is measured and telemetered after having been transformed into a frequency of 5 to 15 kc, corresponding to a current range from 10^{-10}A to 10^{-4}A.

The telemetered signal is decoded and digitized by means of 100 filters. The decoded currents are therefore digitized in steps having a width of about 20%.

The Ni absorbers have thicknesses of 0.762 μ, 0.305 μ, 0.127 μ (respectively 30 μ in., 12 μin., and 5 μ in.). We shall denote them respectively as absorbers #1,#2 and #3. The telescopic factor for these three absorbers is nominally 8.13×10^{-3} cm^2 ster. The true telescopic factors might be slightly different from the above for the following reasons:

1. The gold surface changes with the absorber and does not cover exactly the same area for each wheel position. Thus, a maximum deviation of 5% from the nominal value is possible.

2. The epoxy which keeps the Ni absorbers in place reduces the geometric factor in a way not identical for the three absorbers. Another error of a few percent is thus added.

The scattering efficiency for protons is much smaller than for electrons. From theoretical considerations and by using measurements of protons made with this same instrument operating in a different mode (not considered here), we can see that the protons cannot produce an observable current in the photomultiplier except for that which can be eliminated as background.

The background is determined by measuring the current in the photomultiplier when an Al disk 1 g/cm^2 thick replaces the Ni absorbers. The background current is nearly omnidirectional and is presumably due to electrons with energy greater than 2 Mev, to protons with more than 20 Mev, and to electromagnetic radiation. This current is subtracted from the three currents measured in the scatter mode.

Calibration and in-flight calibration. The detector was calibrated with an electron beam in the energy range of 6 to 160 kev. Figure 3 shows the sensitivity of the instrument for the three Ni absorbers. The response extrapolated above 160 kev has been confirmed by measurements on a similar detector. The energies at which the sensitivity is 50% of its maximum value are 26 kev, 20 kev and 14 kev, respectively for the three absorbers, and it can be seen that the detector is best able to measure the electron energy spectrum in the range from 10 to 40 kev. The telescopic factor has been calculated for the flight unit as $8.13 \times 10^{-3} cm^2$ ster. Later, we measured the acceptance solid angle. Figure 4 shows the calibration performed on the prototype unit. The theoretical 24° for the angle 2 φ of Figure 2 is in agreement with the observations of Figure 4. The finite size of the calibrating source increases the width of the laboratory response curve by 4°. It also was possible to check the performance of the detector during the flight by means of two radioactive sources placed on two wheel positions. Figure 5 shows the 8th dynode current as measured during the flight and as expected from extrapolation of measurements before the flight (the data for this figure were taken only when the background was less than 10%. The results show that the detector sensitivity may have increased at the lower current but was nevertheless stable to within 20% for the period under study.

COORDINATES

We make use of the McIlwain's coordinates L and B/B_o [McIlwain, 1961]. Furthermore, the local pitch angle α_L is used because the detector is directional.

One coordinate can be eliminated by using the Liouville theorem and the constancy of the first adiabatic invariant. We have

$$\frac{\sin^2 \alpha_o}{B_o} = \frac{\sin^2 \alpha_L}{B}$$

where α_o is the pitch angle at the equator. Thus we employ as coordinates L and α_o .

Moreover, we set the following limitations:

1. $2 \leq L \leq 10$: At $L < 2$ the background current becomes comparable with the electron current.

2. $B/B_o < 2$: We study only particles which have been measured near the equator. Any deviation of the real geomagnetic field from the calculated Jensen and Cain field will affect the value of α much more off the equator. At the equator a field deviation will change L; still, for a given L shell the data will be ordered according to α_o if the time variations of the geomagnetic field are not too large.

EXPERIMENTAL DATA

Figures 6 and 7 show the data for the first four orbits considered. The net current for the absorber #1 is shown against α_o at various values of L after the background current has been subtracted. The digitalization of the measurements due to the comb filters is very evident. The straight

lines of Figures 6 and 7 represent least-square fits to the data. Of each triad of lines, the upper one always refers to the current with absorber #3, the middle line with absorber #2, and the lower line with absorber #1. The data points obtained with absorber #2 are shown in the figures. The typical rms error for a least square fit is about 10 to 15%.

Because of limiting to $B/B_o < 2$, all the data - even at high L values - are only functions of L, α_o and of the time.

Figure 8 shows the profiles of the radiation belt for the eight orbits at $\alpha_o = 45°$. The data points indicated by I_1 and I_3 were computed at $\alpha_o = 45°$ from the least-square-fit lines, respectively, for the absorber #3 and #1. I_b is the background current, nearly independent of α_o.

The contribution of the high-energy outer belt electrons to I_b is evident at $L \approx 5$. In this region of space, I_b is sometimes comparable with I_1 and I_3.

It is clear from figure 8 that, for the time of this study, the region below 3 or 4 earth radii is relatively stable whereas the region at higher L is characterized by large changes in electron intensity which occur in times shorter than our sampling period, i.e. the satellite orbit period.

ANALYSIS OF THE DATA

Spectral parameters

We indicate with I_1, I_2, I_3 the net currents (amperes) related to the three absorbers respectively. The ratios $R_1 = I_3/I_1$ and $R_2 =$

I_3/I_2 are useful quantities for investigating the hardness of the spectrum (i.e., how it depends on space and time). Figure 9 shows R_1 versus L at $\alpha_o = 45°$; R_1 was computed from the least-square fits, and no distinction among orbits is made. Figure 10 shows averages and medians obtained from the data in Figure 9 by grouping them in intervals of $\Delta L = 1$. Also, averages and medians for R_2 are shown.

The first result concerning the electron energy spectrum is that the relative number of electrons with energy of the order of 10 to 20 kev is comparatively small for $L < 6$. At 20 kev, from the calibration curves of Figure 3, we have a ratio of 9 between the sensitivities for the thinnest and thickest absorbers. Figure 9 gives $R_1 < 2$ for $L < 6$.

Because of the small energy range investigated, we cannot decide whether the spectrum has a power-law form, exponential form, or any other. Thus, we compute both γ and E_o defined by the differential energy spectra

$$N(E)\,dE = AE^{-\gamma}dE \quad \text{and} \quad N(E)\,dE = N_o e^{-E/E_o}dE$$

(with the usual meaning for the symbols), to present the data in such a way that comparison with different experiments can be made. We use the measured sensitivities σ_i of Figure 3 and compute the ratios

$$R_i = \frac{\int_o^{2\ \text{Mev}} \sigma_3(E)\ E\ N(E)\ dE}{\int_o^{2\ \text{Mev}} \sigma_i(E)\ E\ N(E)\ dE} \quad \text{with } i = 1,2$$

The ratios are only functions of E_o and γ and they are given in Figures 11 and 12.

The solid lines of Figure 13 give E_o and γ obtained from the continuous line of Figure 10. We see, at the same L, that R_1 and R_2 give different E_o and γ values. However, the curves of Figures 11 and 12 were computed on the assumption that the three telescopic factors had exactly the same numerical value. Our previous discussion indicated that they may differ by a few percent.

The broken lines of Figure 13 show E_o and γ after the ratios of Figure 10 have been corrected. For the power-law spectrum perfect agreement is obtained by multiplying R_1 by 0.975 and R_2 by 1.03. For the exponential spectrum we multiply by 0.975 and 1.025, respectively. It should be pointed out that, by making a correction of 5 to 6%, we obtain agreement both for the exponential and the power-law energy spectrum at all the values of L. Thus, it can be concluded that the quantities E_o and γ obtained by means of R_1 are consistent, within the experimental accuracy, with those obtained by using R_2.

Moreover, we now have a reasonable estimate of the systematic error in the determination of the spectral parameters due to the geometry of the instrument and calibration procedure (i.e., from Figure 13, a factor of 2 for E_o at $L = 3$). In what follows, only the uncorrected R_1 will be used because the propagation of the errors to E_o and γ is smaller than that due to R_2.

Spectral parameters versus L, α_o and time. The use of the least-square fit method alone for deriving a simple relation between currents and equatorial pitch angles for a given L and orbit cannot be applied

here in studying the spectral dependency on α_o. The reason is that the spectral parameters are very sensitive to a few percent change in R_1, as we noted previously. Because the fits have an accuracy of a few percent, the R_1 values calculated at various α_o would not be independent, thus yielding spectral parameters whose dependency on α_o would not be genuine.

To compute the quantities E_o and γ as function of L, α_o , and time, we use the following steps:

1. Take the data points I_i (i = 1,3) for a given L and orbit against α_o (as in Figures 6 and 7).

2. Group them in four α_o intervals: 10-30, 30-50, 50-70, and 70-90.

3. For each α_o interval, correct the data to the middle point of the interval by using the slopes of the least square straight lines.

4. For each α_o interval, take the median and the lower and upper quartile of the population made by the corrected data (I_m, I_L, I_u).

5. Take $I_m \pm (I_u - I_L)/2\sqrt{N}$. (N is the number of data points in the population.)

6. Compute $R_1 = I_m{}^{(3)}/I_m{}^{(1)}$ with its error ΔR_1. In order to reduce a possible effect due to the background current I_b, we compute and use only the R_1 values which are affected by less than 10% by the background correction.

7. Compute $E_o \pm \Delta E_o$ and $\gamma \pm \Delta\gamma$ from $R_1 \pm \Delta R_1$ as function of L, orbit, and α_o. ΔE_o and $\Delta\gamma$ have thus the meaning of probable errors.

The results of these calculations are shown in Figures 14 and 14 for orbits 1, 2, 7, and 8; the selection of these orbits is arbitrary. We show only E_o for simplicity, considering that it is much easier to attribute to E_o a physical meaning than to γ. In this case we believe that E_o is a good estimate of the average electron energy (if the energy spectrum were an exponential then the average energy would have been exactly E_o). It must be emphasized that we do not claim, in this region of space and for these particles, that the spectrum is exactly of an exponential nature; we believe that an extrapolation outside the energy range explored here would be dangerous.

The most salient features common to all the data in Figures 14 and 15 are the following:

1. Within the errors there is no dependency of E_o on α_o.

2. Very crudely, E_o decreases with increasing L. However, in some cases E_o shows the tendency to remain constant over a range of 2 or more earth radii.

In addition the data for each individual orbit show some peculiar characteristics which are discussed later.

Omnidirectional intensity. From the data available to us, it is possible to compute at the equator the omnidirectional intensity of electrons with energy greater than a given value E*. We made the following hypothesis:

1. The spectral shape does not depend on α_o; this hypothesis is somewhat supported by the data in Figures 14 and 15.

2. The energy spectrum can be approximated by $dN = N_o e^{-E/E_o} dE$.

The current with the absorber #3, after having subtracted the background, is given by

$$I_3 = N_o \int_o^{2\ \text{Mev}} \sigma_3(E) E e^{-E/E_o}\, dE \quad \text{or} \quad I_3 = N_o\, f(E_o)$$

where $f(E_o)$ is evaluated numerically.

The directional intensity of electrons with energy greater than E* is given by

$$j(>E^*) = \int_{E^*}^{\infty} N_o e^{-E/E_o}\, dE = N_o E_o e^{-E^*/E_o} = \frac{I_3}{f(E_o)}\, E_o e^{-E^*/E_o}$$

From Figures 6 and 7 we see that, with a few percent error, I_3 can be expressed as

$$I_3 = A\, e^{\alpha_o/a}$$

The omnidirectional intensity is

$$J\ (>E^*) = 4\pi \int_o^{\pi/2} j\ (>E^*) \sin \alpha_o\, d\alpha_o$$

or

$$J\ (>E^*) = \frac{AE_o}{f(E_o)}\ e^{-E^*/E_o}\, 4\pi \int_o^{\pi/2} e^{\alpha_o/a} \sin \alpha_o\, d\alpha_o$$

The last integral is resolved analytically. The quantities A, E_o, and a are obtained from data, some of which are shown in Figures 6, 7, 14 and 15. The results of these calculations are shown in Figures 16 and 17 for E* = 10 and 50 kev, respectively.

STATISTICAL AND SYSTEMATIC ERRORS

Before discussing Figures 16 and 17 and comparing them with other experimental results, we shall investigate the nature and order of magnitude of errors and approximations involved in this analysis.

Statistical errors. These errors appear to be fully expressed by the scattering of the points in Figures 16 and 17. We distinguish two kinds of statistical errors:

1. Those arising from the least-square fit of currents versus α_o: We use the same fit for all the α_o values. However, the fits and the data populations are different at a different L value and orbit. Therefore, for a given orbit the comparison of $J_{I,t}(>E^*)$ with the $J_{L\pm\Delta L,t}(>E^*)$ in the vicinity of L gives an estimation of errors arising from bad fits.

2. Those arising from the computation of E_o from R_1: In Figures 14 and 15 such statistical errors are expressed by the vertical bars. In Figures 16 and 17 they can be estimated reasonably by the scattering of the points at different α_o for the same L and orbit.

Systematic errors. The most important error in the computation of E_o is that due to the uncertainty in geometric factors. From Figure 13

and from previous considerations, we have: for $E_o \approx 200$ kev, an uncertainty by a factor of 2; for $E_o \approx 20$ kev, about 30%. Also, the calibration curves of Figure 3 are affected by some error; however, they were well reproducible from one day to the next and, within reasonable deviations, from one detector to another. Only relative systematic errors can change E_o. We estimate these errors to be less than 1%. Thus, we might increase the uncertainty on E_o by about 20%.

Referring to Figures 16 and 17, we must consider the error introduced by the hypothesis of an exponential spectrum. In order to have some indication about such an error, we computed the omnidirectional intensity by making use of a power-law spectrum. We obtained, for electrons with energy greater than 50 kev, an intensity always greater, by a factor of between 1.5 and 3, than that shown in Figure 17 at values of E_o from 10 to 100 kev (corresponding to γ values between 2.96 and 1.15). The same thing holds for electrons with energy greater than 10 kev.

Finally, we consider the error arising from a possible gain change during the flight (Figure 5). This seems to be the only systematic error which tends to increase the calculated omnidirectional intensity. If we take it into account, we obtain an intensity lower by 10 to 20%.

Therefore, the omnidirectional intensity we have computed probably represents a lower limit with regard to the approximations involved in these calculations.

COMPARISON WITH OTHER EXPERIMENTAL RESULTS

The omnidirectional intensity we computed can be compared with that measured by Frank et al.[1963, 1964]. We have calculated the peak intensity at orbit 1 for electrons with energy greater than 40 kev and found 1.0×10^9 electrons/cm^2/sec. Frank et al. [1963, 1964] give 2×10^8 electrons/cm^2/sec with an instrument on this same satellite, at the same time and position in space. The discrepancy can be explained as follows: Our intensity may be decreased by 20% if we take into account a possible gain change during the flight (Figure 5). On the other hand, the 213 Geiger counter of Frank et al. operates in a saturated mode and does not have a sharp cutoff at 40 kev. Taking into account these two effects, the 213 Geiger tube is probably responding to $\approx 6 \times 10^8$ electrons/cm^2/sec above 40 kev [Frank, L.A., private communication, 1964].

The energy flux we detected can be compared with that detected by Freeman [1964], employing CdS crystals. For orbit 1 we have at L $\approx$ 5 about 150 ergs/cm^2/sec and, at L $\approx$ 8, about 30 ergs/cm^2/sec. On the day side of the earth Freeman observes fluxes of the order of 10 to 100 ergs/cm^2/sec between 16,000 km radial distance and the geomagnetic boundary - in general agreement with our fluxes, considering that our orbit 1 data gives the maximum value for the period studied.

Our data show that there is a region of trapped electrons with an average energy of about 10 kev and a peak intensity of about 10^9 electrons/cm^2/sec at L $\approx$ 8, both the peak intensity and position in L strongly varying with time. These electrons are trapped because:

1. They exist well inside the boundary of the magnetosphere (during orbit 1, the boundary was at $L \approx 11$ [Frank et al., 1963]).

2. They have a pitch angle distribution of the kind one has for trapped particles (see Figures 6, 7, and 18).

It should be pointed out that these electrons show a discontinuity in the energy spectrum with respect to those at lower L values (Figures 14 and 15); therefore, we suggest that they should not be regarded as a tail of the more energetic ones as far as origin and life are concerned. We see them in orbit 1, almost disappearing in orbit 2. During orbit 8 they are present at $L \approx 9$-10; they are also visible in Figure 8 and in the Geiger counter measurements of Frank et al. [1963].

We believe that these electrons are probably related to those discovered by Gringauz et al. [1960a, 1960b, 1964], with the apparatus aboard Lunik I, constituting his "outermost belt" of charged particles. Gringauz detects about 2×10^8 electrons/cm^2/sec, somewhat lower than our peak values but at a different time. With Lunik I measurements on January 2, 1959, at the same distance from the subsolar point as our measurements, the inner boundary of his belt was approximately at $L \approx 5$ at a geomagnetic latitude of $\approx 20°$ [Gringauz et al., 1960a, 1960b] thus, presumably, inside the boundary of the magnetosphere.

Relation with the Auroras

Figure 18 shows the pitch angle distribution of electrons at $L = 8$ during orbit 1. With $E_o \simeq 10$ kev $\simeq$ constant at all values of α_o (see Figure 14), we can compute the directional intensity

$$N_o(\alpha_o) = \frac{I_3(\alpha_o)}{f(10\ \text{kev})} = \frac{I_3(\alpha_o)}{8 \times 10^{-16}} \quad \text{electrons/(cm}^2\text{sec ster kev)}$$

It is interesting to compute the extrapolated total number of particles which are in the loss cone. We have:

$$J(\text{dumped}) = 2\pi N_o\ (\alpha_o = 0)\ E_o e^{\frac{-5\ \text{kev}}{E_o}} \simeq 0.3 \times 10^9 \text{ electrons/cm}^2 \text{ sec}$$

with energy above 5 kev. McIlwain [1960] gives for a brilliant aurora a flux of 5×10^{10} electrons/(cm^2 sec ster). Davis et al. [1960] for an Intensity I aurora give a flux of the order of 10^9 electrons/cm^2/sec. This shows that equatorial electrons of the kind shown in Figure 18 are sufficient to produce a very weak aurora. It is of interest to compute for how long time this reservoir of electrons would maintain a bright aurora.

The tube of force along L = 8 having a 1-cm^2 section at the earth's surface has a volume of about 2.1×10^{12} cm^3. The measured omnidirectional intensity of the electrons with energy greater than 5 kev is 2×10^9 electrons/cm^2/sec. The corresponding electron density is 0.45 electron/cm^3 which gives 10^{12} electrons inside the tube of force. If all these electrons are dumped at once, we have just one very brilliant aurora lasting only for a time of the order of a few seconds. Thus, our measurements support the O'Brien's "splash catcher" model [O'Brien, 1962].

Finally, it is of interest to compute the ratio between the energy density of these electrons and that of the geomagnetic field. The electron energy density is $\approx 6 \times 10^{-9}$ erg/cm^3 at L = 8. The earth's magnetic field energy density measured at L = 8 on the same satellite and at the same time [Private communication L. J. Cahill] is approximately 6×10^{-8} erg/cm^3. Thus we obtain a ratio of 0.1 which shows that the geomagnetic field is heavily loaded by the 10 kev electrons. This is comparable with the energy density of >100 kev protons measured by this region [Davis and Williamson, 1963].

Acknowledgements. We are grateful to R. A. Hoffman and A. Konradi for their useful discussions, and we thank J. H. Trainor for performing the calculations shown in Figure 4.

REFERENCES

Davis, L. R., O. E. Berg, and L. H. Meredith, Direct Measurements of particle fluxes in and near auroras, Proc. First International Space Science Symposium, Nice, 1960, pp. 721-735, 1960.

Davis, L. R., and J. M. Williamson, Low-energy trapped protons, Space Research III, ed. W. Priester (Amsterdam, North-Holland Publishing Co, 1963) 365.

Frank, L. A., J. A. Van Allen, W. A. Whelpley, and J. D. Craven, Absolute intensities of geomagnetically trapped particles with Explorer XIV, J. Geophys. Res., 68, 1573-1579, 1963.

Frank, L. A., J. A. Van Allen, and H. K. Hills, An experimental study of charged particles in the outer radiation zone, Report 64-1, State University of Iowa, Iowa City, Iowa, 1964.

Freeman, John W., Jr., The morphology of the electron distribution in the outer radiation zone and near the magnetospheric boundary as observed by Explorer XII, J. Geophys. Res., 69, 1691-1724, 1964.

Gringauz, K. I., V. G. Kurt, V. I. Moroz, and I. S. Shklovskii, Results of observations of charged particles observed out to R ~ 100,000 km, with the aid of charged-particle traps on soviet space rockets, Astron. Zh., 37, 716-735, 1960.

Gringauz, K. I., V. G. Kurt, V. I. Moroz, and I. S. Shklovsky, Ionized gas and fast electrons in the earth's neighborhood and in interstellar space, Dokl. Akad. Nauk SSSR, 132(no. 5), 1062-1065, 1960.

Gringauz, K. I., Remarks on papers by J. W. Freeman, J. A. Van Allen, L. J. Cahill, and by L. A. Frank, J. A. Van Allen, and E. Macagno. J. A. Van Allen, Remarks on letter by K. I. Gringauz, J. Geophys. Res., 69, 1007-1013, 1964.

McIlwain, C. E., Direct measurement of particles producing visible aurora, J. Geophys. Res., 65, 2727-2774, 1960.

McIlwain, C. E., Coordinates for mapping the distribution of magnetically trapped particles, J. Geophys. Res., 66, 3681-3691, 1961.

O'Brien, B. J., Lifetimes of outer-zone electrons and their precipitation into the atmosphere, J. Geophys. Res., 67, 3687, 1962.

FIGURE CAPTIONS

Fig. 1. Time and space covered in this study.

Fig. 2. Schematic drawing of the electron detector in the scatter geometry mode.

Fig. 3. Calibration of the electron detector for the scatter geometry mode.

Fig. 4. Angular response of a prototype detector to a Ni^{63} 100μC radioactive source.

Fig. 5. The dots are source responses measured in orbit. The lines are the predicted responses based on pre-launch measurements.

Fig. 6. Current versus equatorial pitch angles at various L, orbits 1 and 2, after subtracting the background.

Fig. 7. Current versus equatorial pitch angles at various L, orbits 3 and 4, after subtracting the background.

Fig. 8. Current at an equatorial pitch angle of 45° for all orbits and L shells under study. The current I_2 with the #2 absorber is not shown; it is always $I_1 < I_2 < I_3$.

Fig. 9. The quantity $R_1 = I_3/I_1$ at $\alpha_o = 45°$ versus L; no discrimination is made among orbits.

Fig. 10. Averages and medians obtained from Figure 9. (The errors denote standard deviations.)

Fig. 11. Relation between $R_1 = I_3/I_1$ and $R_2 = I_3/I_2$ and E_o under the assumption of an exponential energy spectrum. Numerical integrations were performed by making use of the measured sensitivity shown in Figure 3.

Fig. 12. Same as Figure 11, for assumed power-law energy spectrum.

Fig. 13. E_o and γ versus L as obtained from the averages of Figure 10. The solid lines show disagreement at a given value of L between E_o and γ obtained from R_1 and those obtained from R_2. The broken lines show E_o and γ after the telescopic factors have been corrected; the correction is made in such a way to obtain agreement between results from R_1 and from R_2. This figure shows that the E_o and γ computed by means of R_1 are in agreement with those computed by means of R_2 within the experimental accuracy. It also shows that the resolution is not sufficient to distinguish between an exponential and a power-law energy spectrum.

Fig. 14. E_o versus L at various α_o for orbits 1 and 2.

Fig. 15. E_o versus L at various α_o for orbits 7 and 8.

Fig. 16. Omnidirectional intensity at the equator of electrons with energy greater than 10 kev for all orbits and L shells under study. The points at the same L and orbit and different L are completely independent from each other.

Fig. 17. Same as Figure 16, for electrons with energy greater than 50 kev.

Fig. 18. Pitch angle distribution of equatorial electrons ($B/B_o < 2$) during orbit 1 at L = 8. These electrons have an energy spectrum independent of α_o and softer than that in the region of the outer belt. (see Fig. 14)

TABLE I. Main Orbital Characteristics of Explorer XIV

Launch date and time (U. T.)	October 3, 1962, at $04^h\ 12^m$
Perigee, Km Altitude	280
Apogee, radial distance	104,870 km $\approx$ 16.5 earth radii
Inclination, deg	33
Period	$36^h\ 24^m$
Spin period, sec	≈ 6
Total precession angle, deg	between 0 and 70
Precession period, sec	≈ 4

EXPLORER XIV
SELECTED DATA

$\frac{B}{B_o} < 2 \qquad 2 \leq L \leq 10$

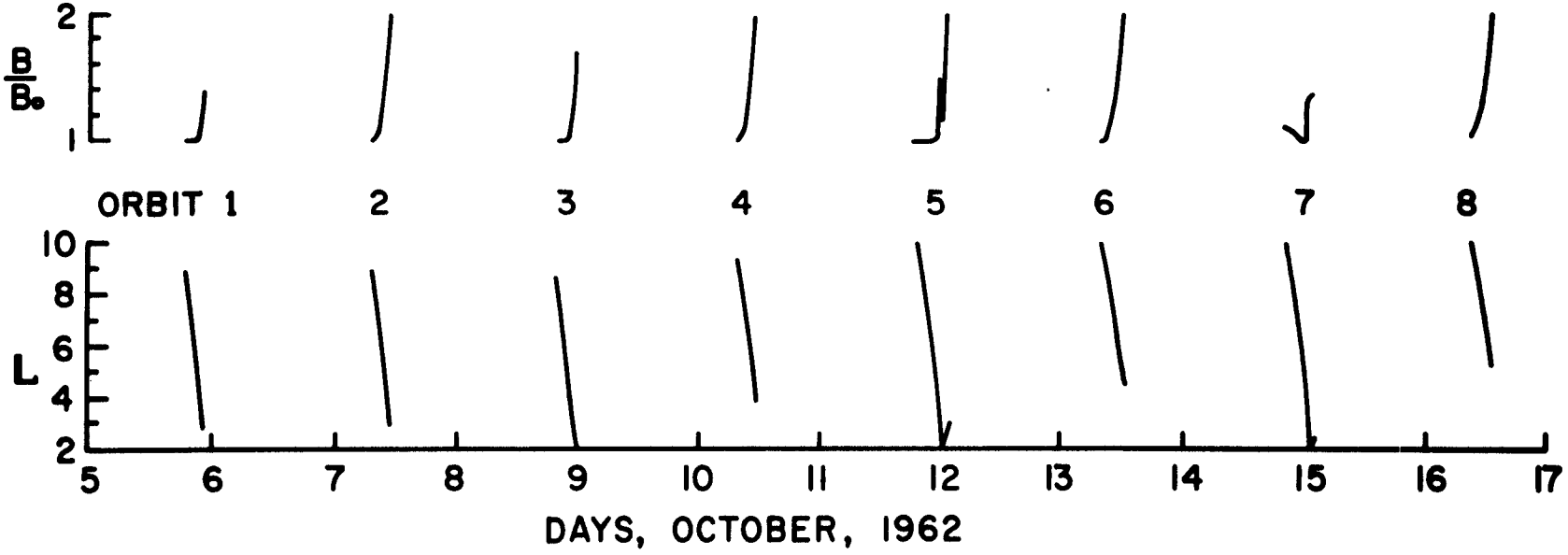

SCATTER GEOMETRY

$\Phi = 12°$

$\Omega = 0.035$ STERADIANS

TF = 8.13×10^{-3} CM^2 STERD.

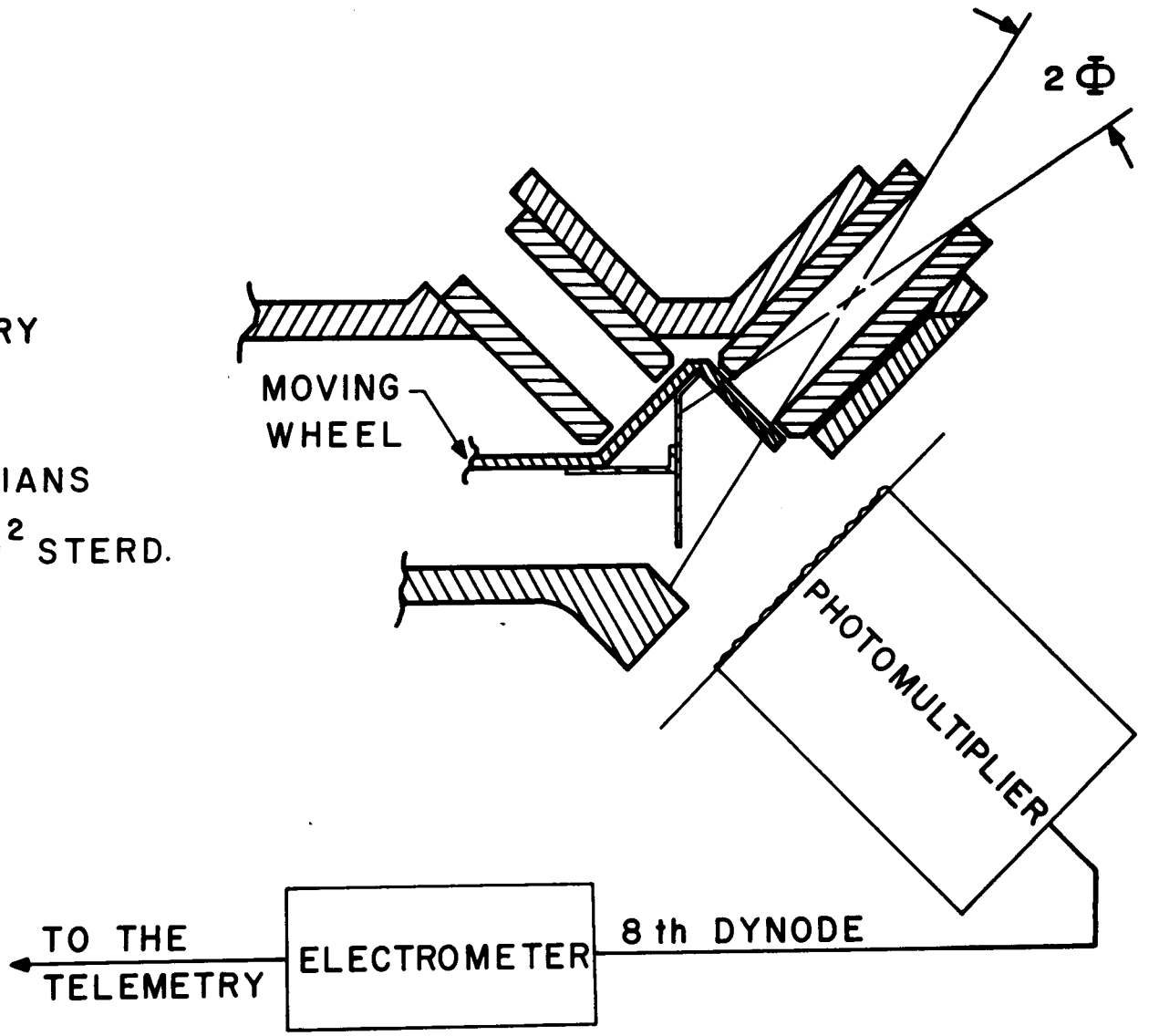

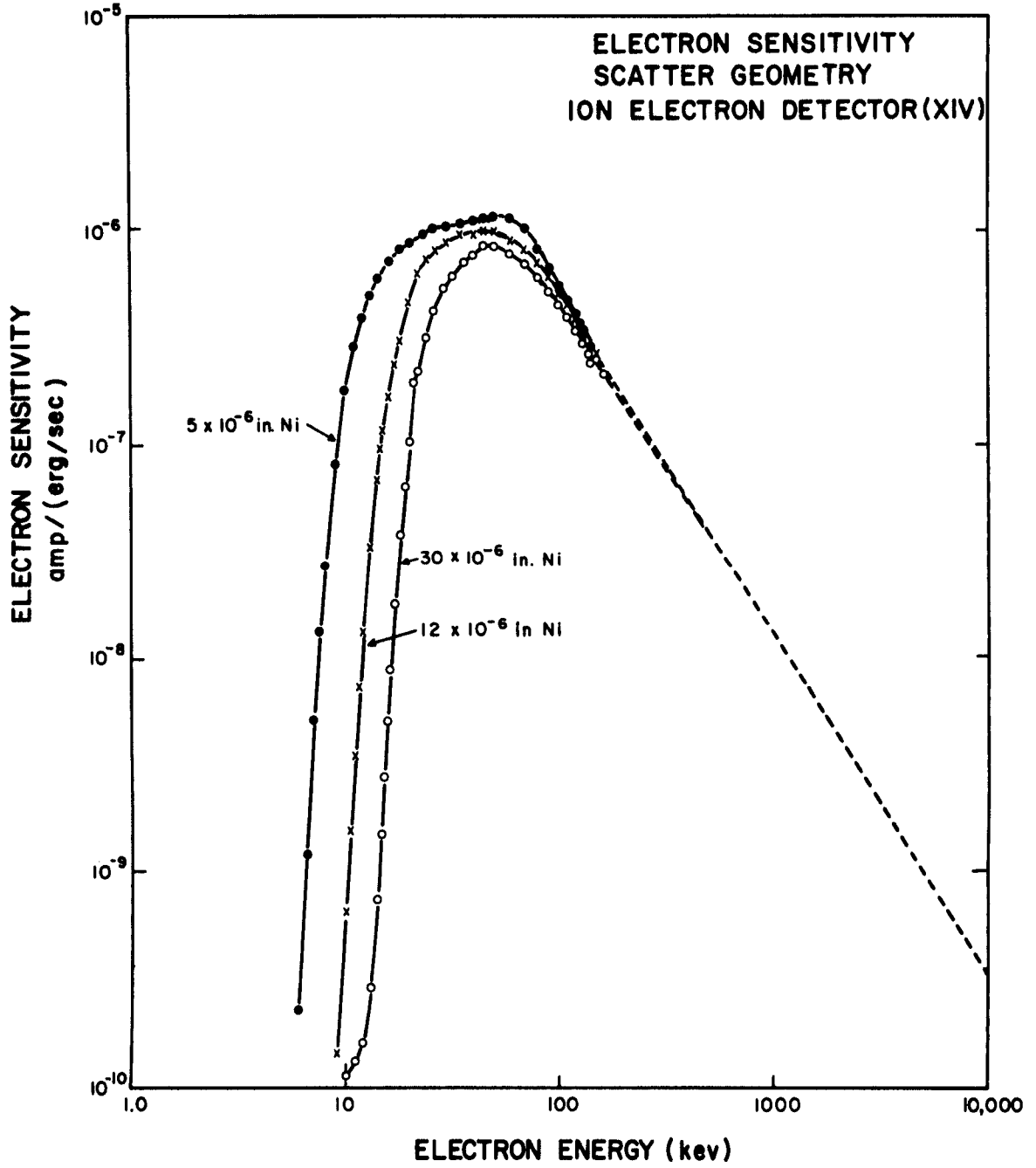
ELECTRON SENSITIVITY
SCATTER GEOMETRY
ION ELECTRON DETECTOR (XIV)
ELECTRON SENSITIVITY
amp/(erg/sec)
10^{-5}
10^{-6}
10^{-7}
10^{-8}
10^{-9}
10^{-10}
5 x 10^{-6} in. Ni
30 x 10^{-6} in. Ni
12 x 10^{-6} in Ni
1.0
10
100
1000
10,000
ELECTRON ENERGY (kev)

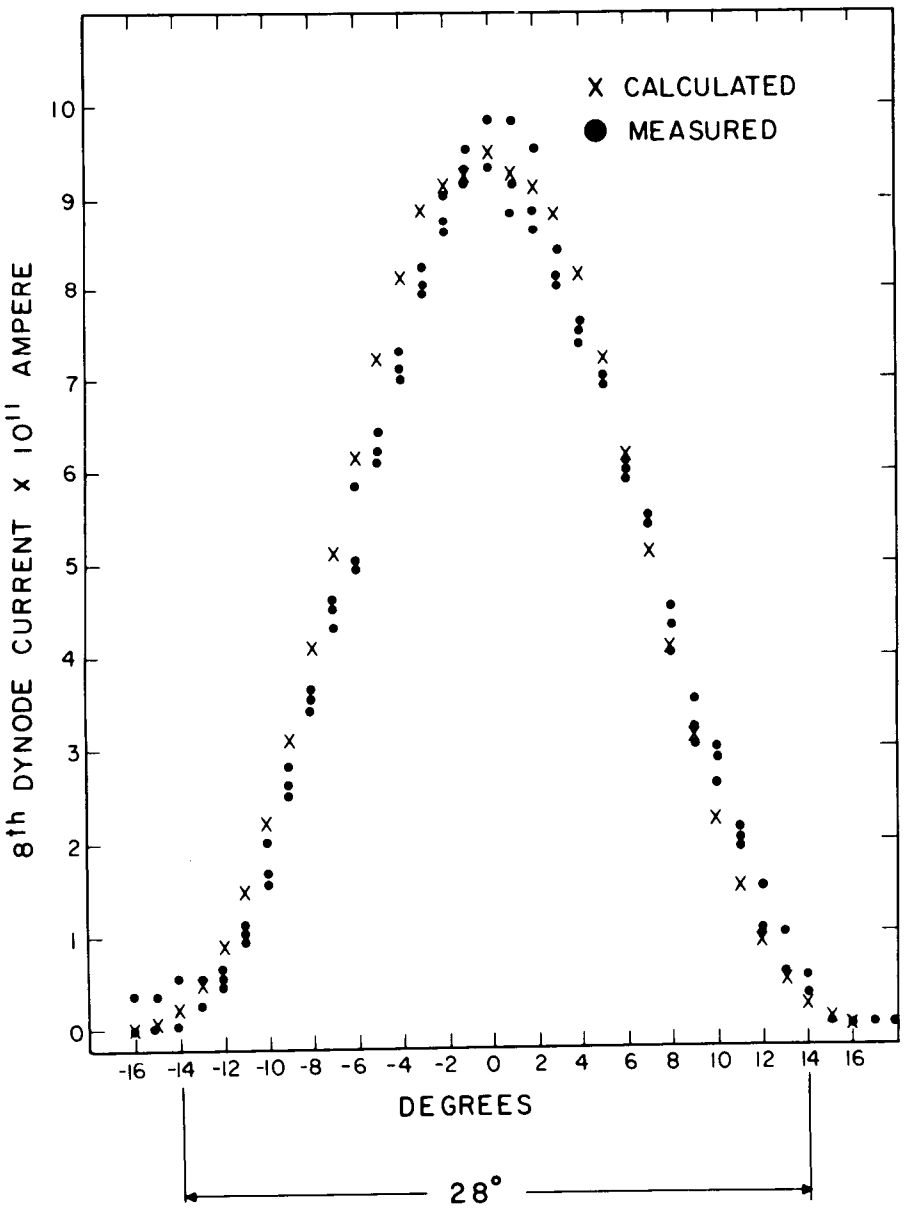

SCATTER GEOMETRY

ANGULAR RESPONSE

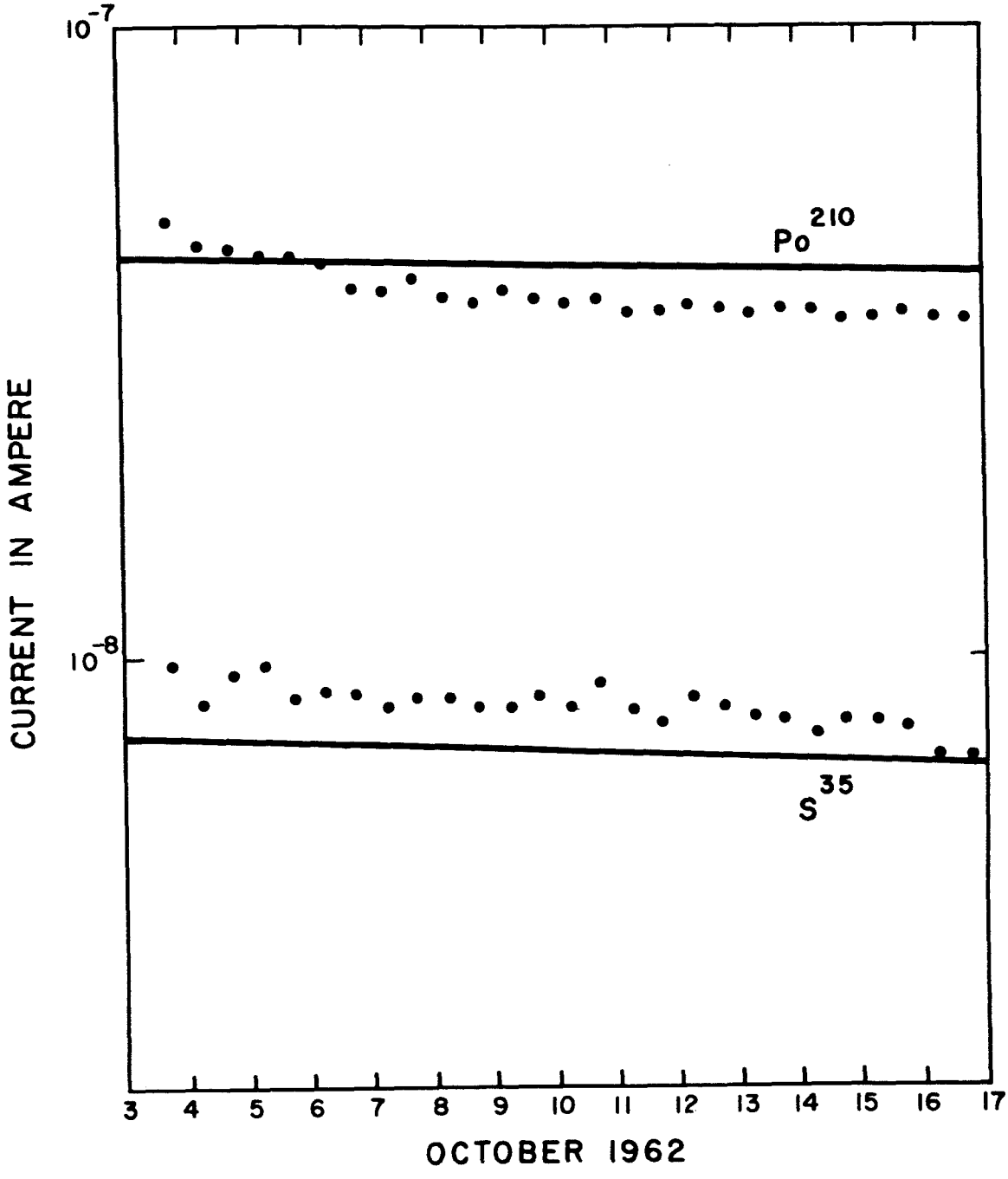
10^{-7}
10^{-8}
CURRENT IN AMPERE
Po^{210}
S^{35}
3 4 5 6 7 8 9 10 11 12 13 14 15 16 17
OCTOBER 1962

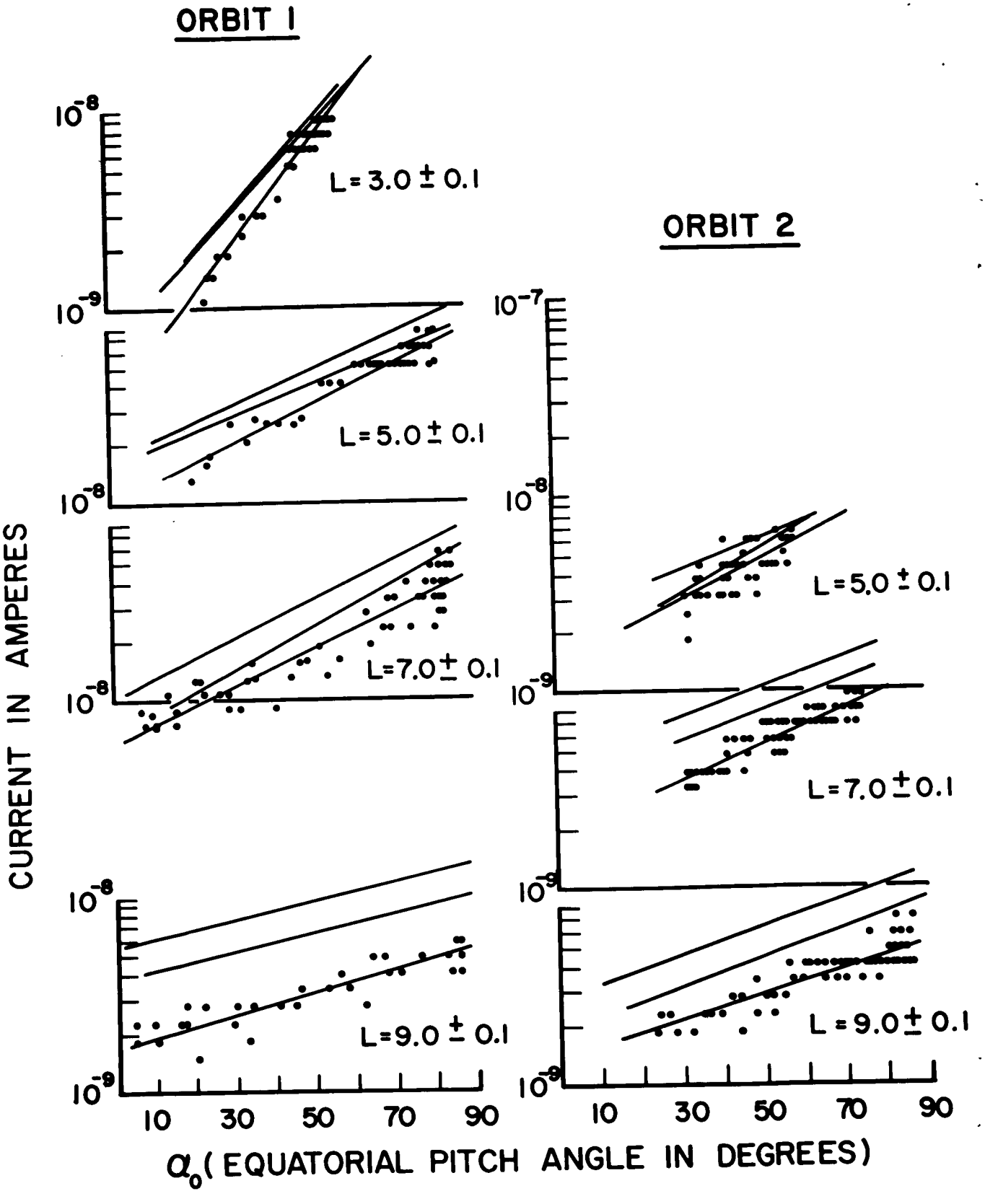
ORBIT 1
ORBIT 2
L=3.0 ± 0.1
L=5.0 ± 0.1
L=7.0 ± 0.1
L=9.0 ± 0.1
L=5.0 ± 0.1
L=7.0 ± 0.1
L=9.0 ± 0.1
CURRENT IN AMPERES
10 30 50 70 90
α0 (EQUATORIAL PITCH ANGLE IN DEGREES)

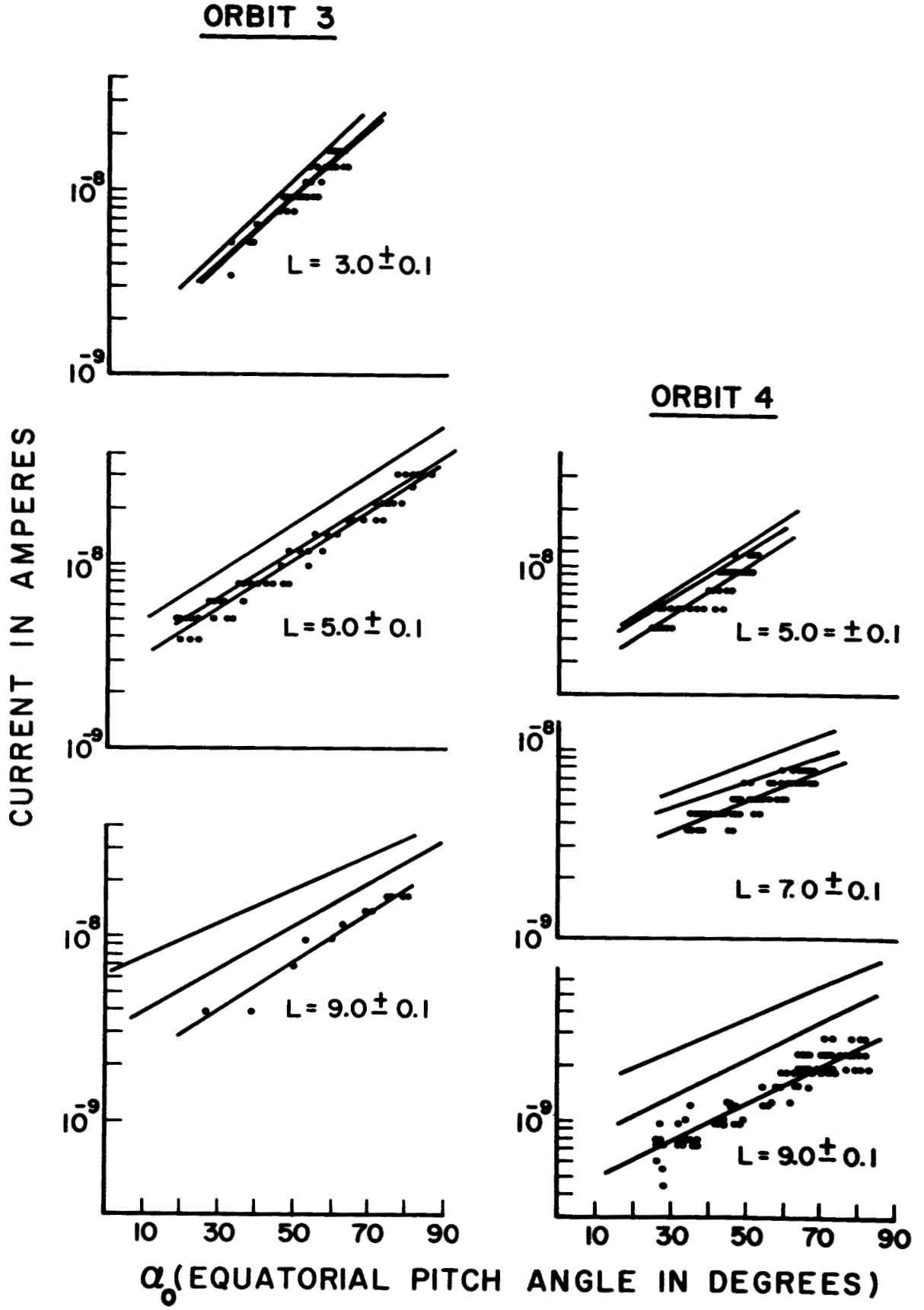
ORBIT 3
ORBIT 4
CURRENT IN AMPERES
10^{-8}
10^{-9}
L = 3.0 ± 0.1
L = 5.0 ± 0.1
L = 9.0 ± 0.1
L = 5.0 = ± 0.1
L = 7.0 ± 0.1
L = 9.0 ± 0.1
10
30
50
70
90
α_0 (EQUATORIAL PITCH ANGLE IN DEGREES)

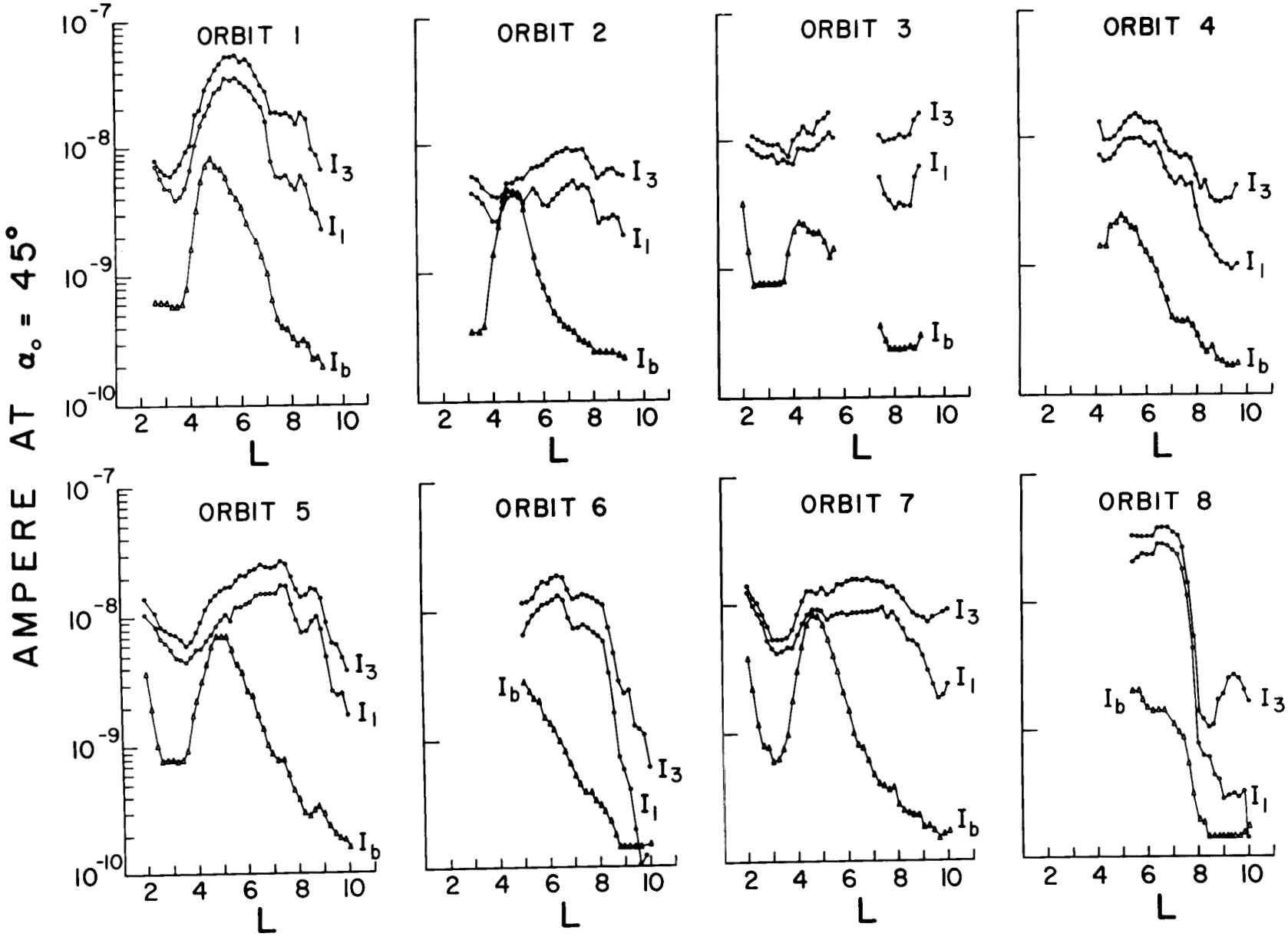
AMPERE AT α_o = 45°
ORBIT 1
ORBIT 2
ORBIT 3
ORBIT 4
ORBIT 5
ORBIT 6
ORBIT 7
ORBIT 8
10^{-7}
10^{-8}
10^{-9}
10^{-10}
I_3
I_1
I_b
2 4 6 8 10
L

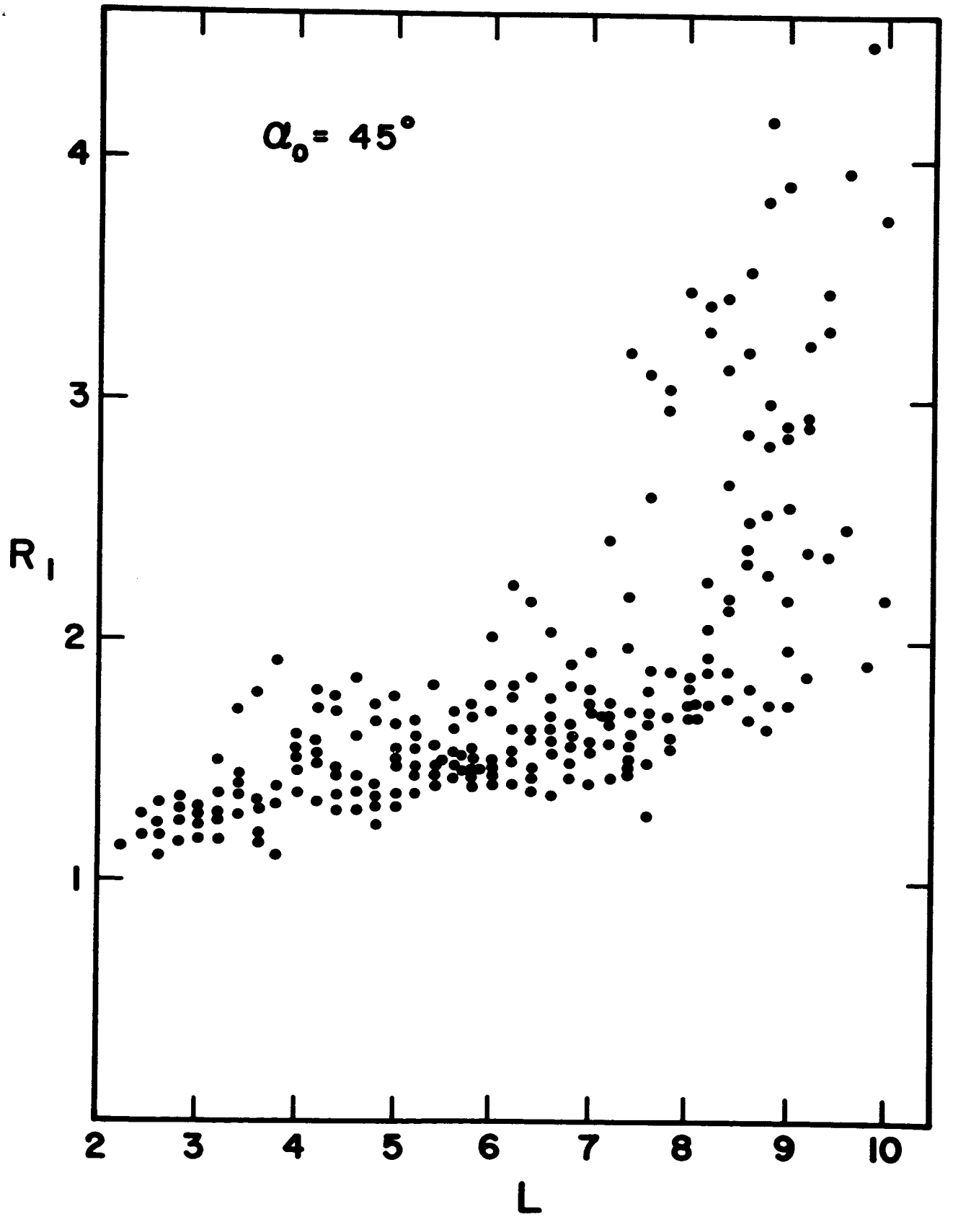
$\alpha_0 = 45°$
R_1
4
3
2
1
2
3
4
5
6
7
8
9
10
L

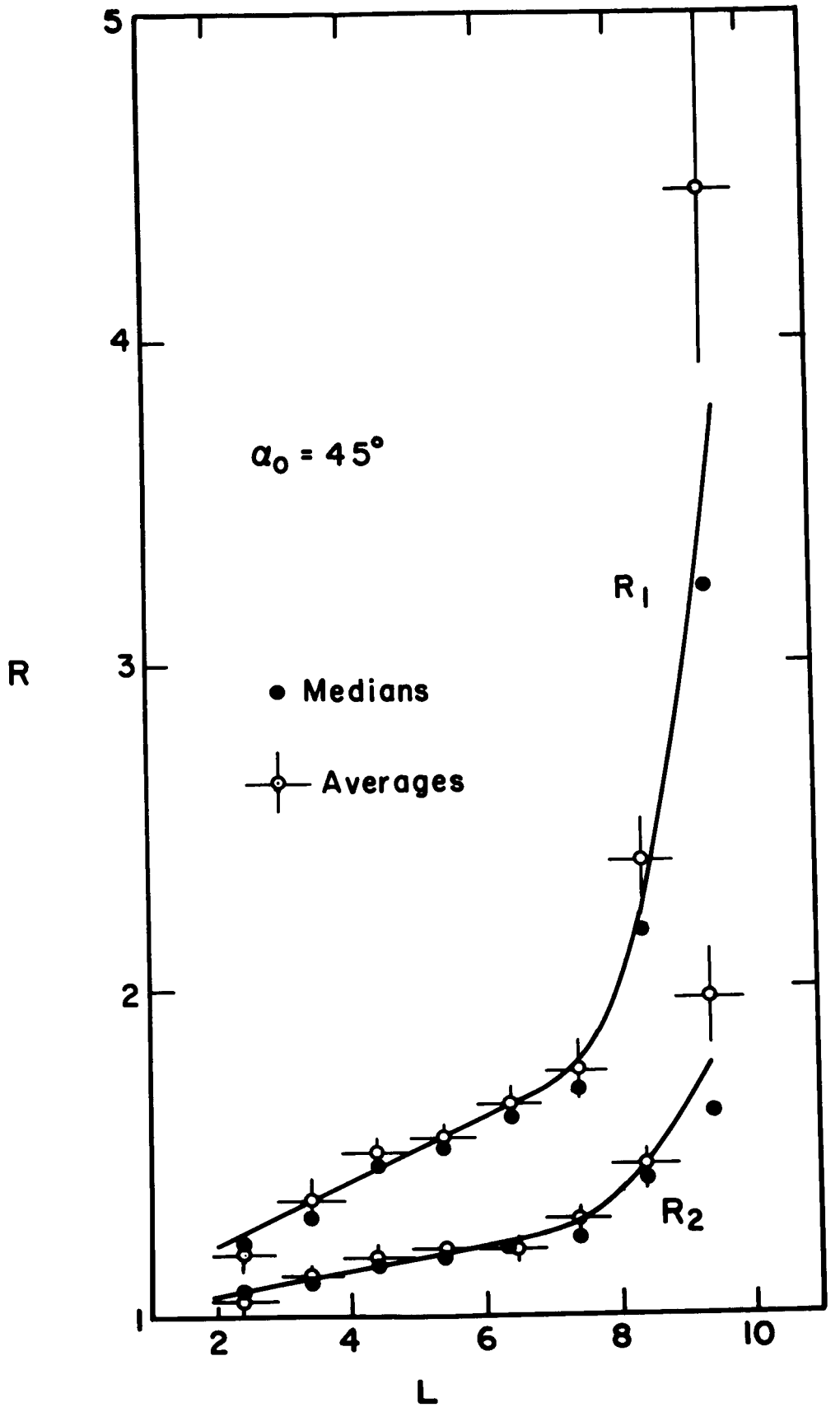
5
4
3
2
1
R
$\alpha_0 = 45°$
R_1
R_2
Medians
Averages
2
4
6
8
10
L

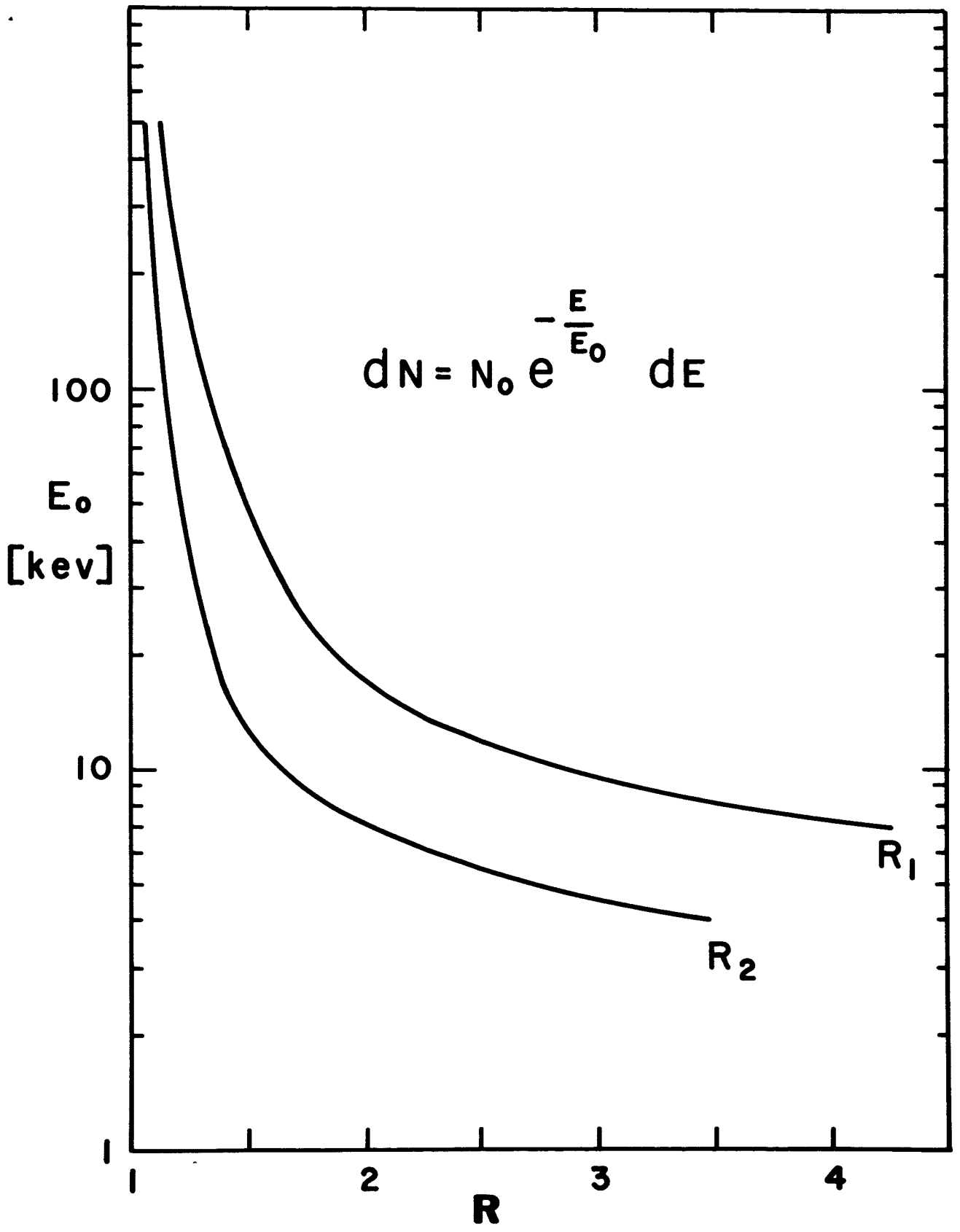
$dN = N_0 e^{-\frac{E}{E_0}} dE$
100
10
1
E_0
[kev]
1
2
3
4
R
R_1
R_2

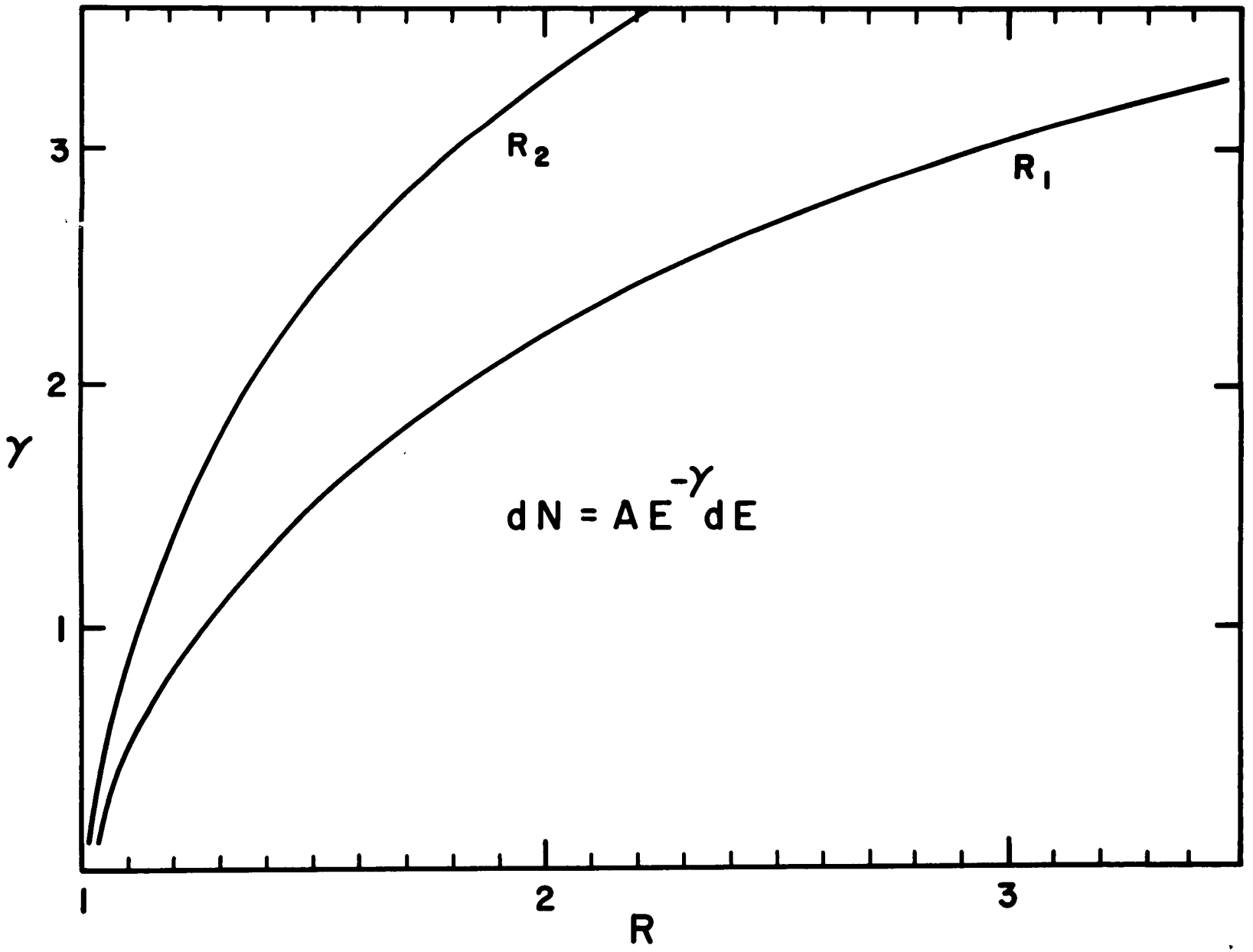
3
2
1
γ
R₂
R₁
dN = AE^-γ dE
1
2
3
R

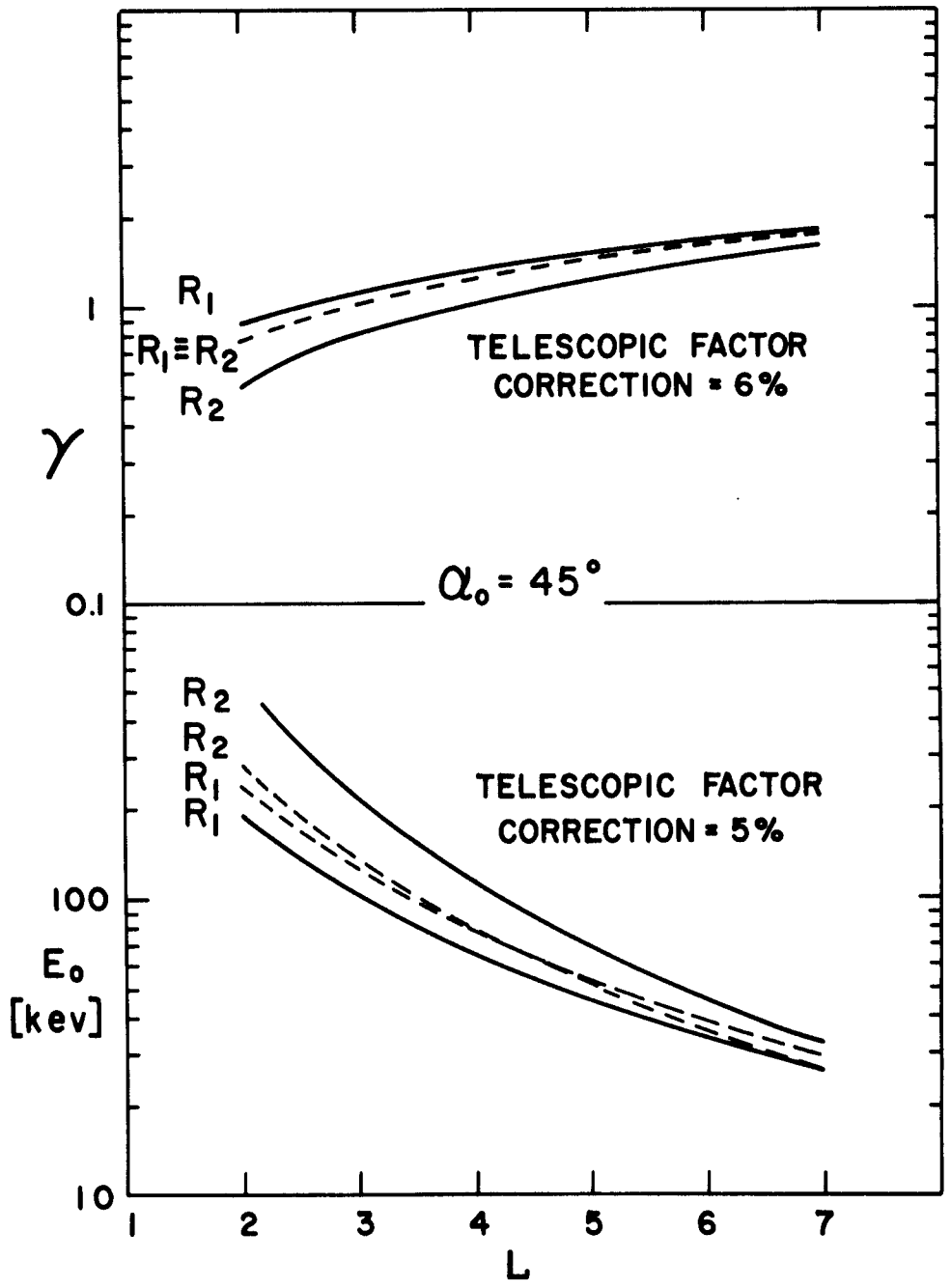
1
0.1
γ
R1
R1≡R2
R2
TELESCOPIC FACTOR
CORRECTION = 6%
α0 = 45°
R2
R2
R1
R1
TELESCOPIC FACTOR
CORRECTION = 5%
100
E0
[kev]
10
1
2
3
4
5
6
7
L

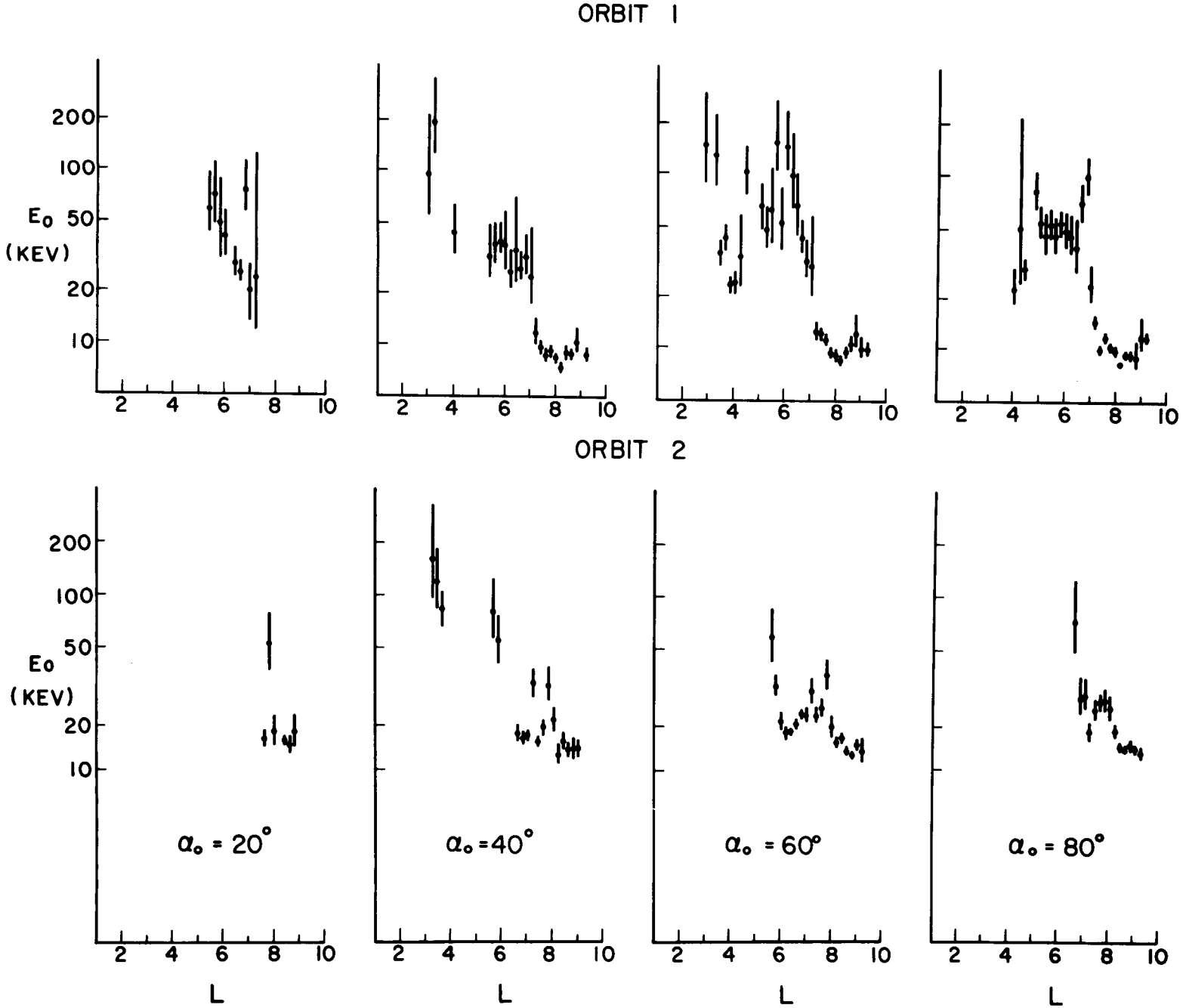
ORBIT 1
ORBIT 2
E_0 (KEV)
200
100
50
20
10
2
4
6
8
10
L
α_o = 20°
α_o = 40°
α_o = 60°
α_o = 80°

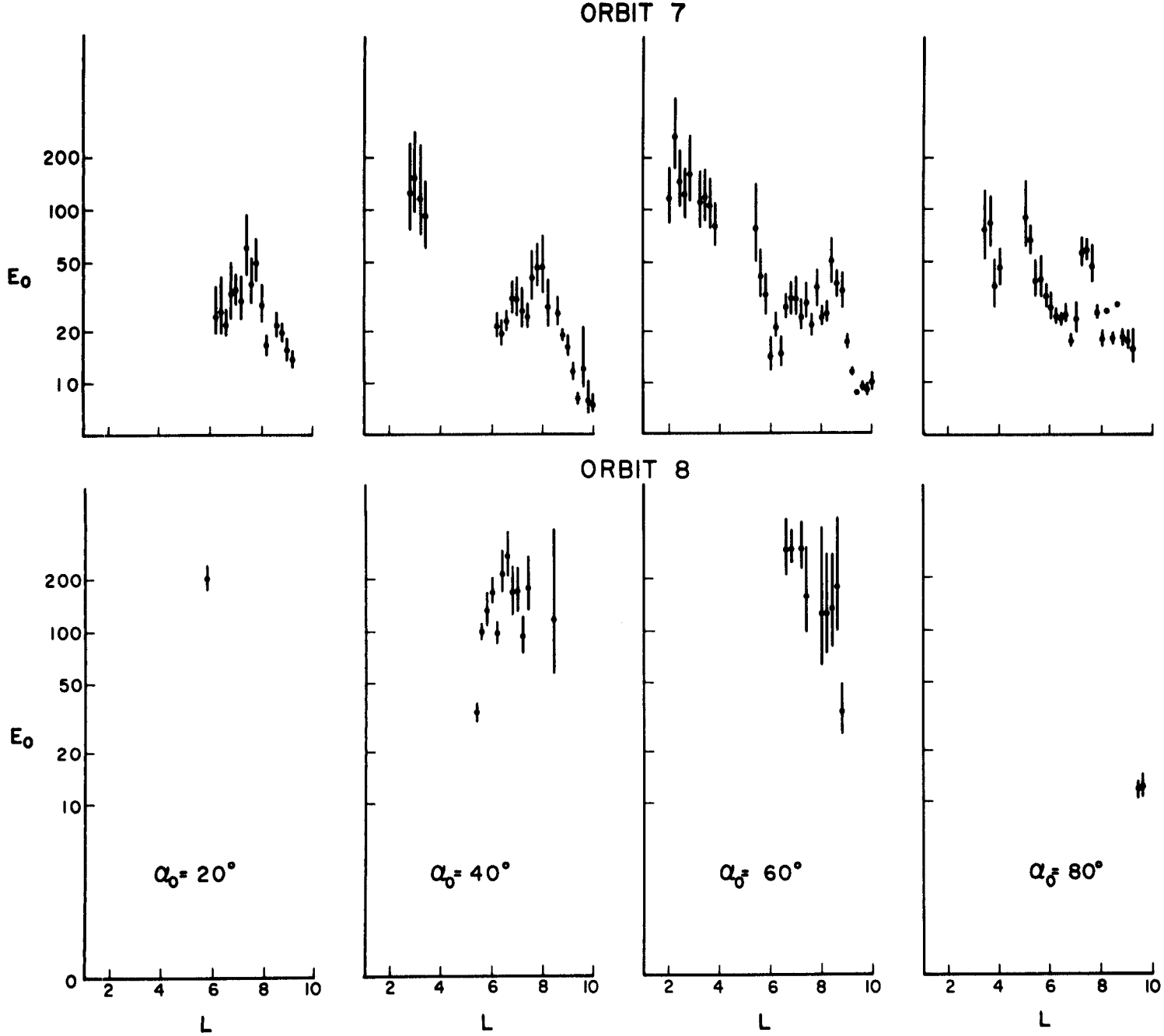
ORBIT 7
ORBIT 8
E_0
200
100
50
20
10
0
2
4
6
8
10
L
$\alpha_0 = 20°$
$\alpha_0 = 40°$
$\alpha_0 = 60°$
$\alpha_0 = 80°$

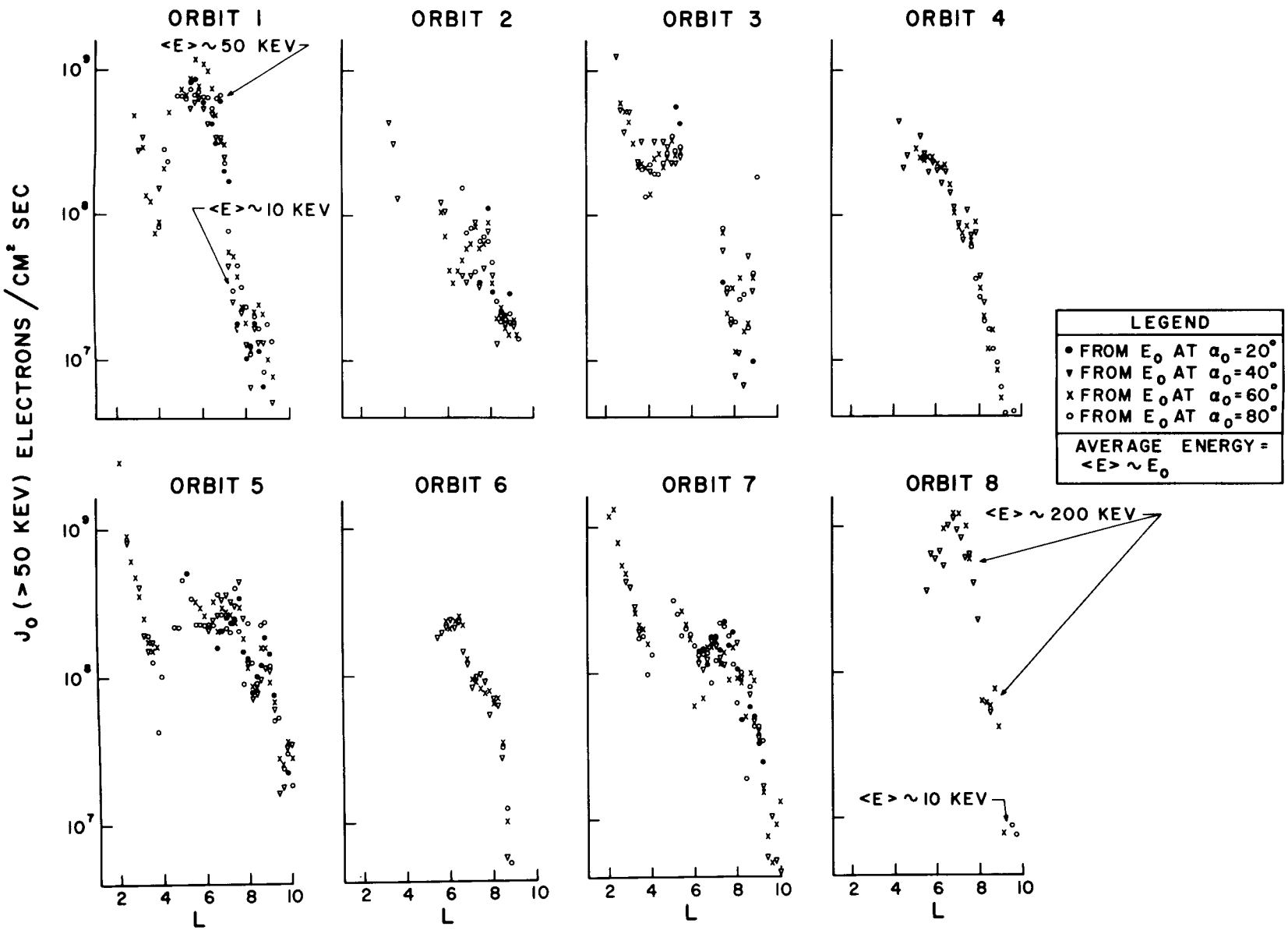
ORBIT 1
ORBIT 2
ORBIT 3
ORBIT 4
ORBIT 5
ORBIT 6
ORBIT 7
ORBIT 8
<E> ~ 50 KEV
<E> ~ 10 KEV
<E> ~ 200 KEV
<E> ~ 10 KEV
J_0 (> 50 KEV) ELECTRONS /CM² SEC
10^9
10^8
10^7
2 4 6 8 10
L
LEGEND
• FROM E_0 AT $\alpha_0 = 20°$
▾ FROM E_0 AT $\alpha_0 = 40°$
x FROM E_0 AT $\alpha_0 = 60°$
○ FROM E_0 AT $\alpha_0 = 80°$
AVERAGE ENERGY = <E> ~ E_0

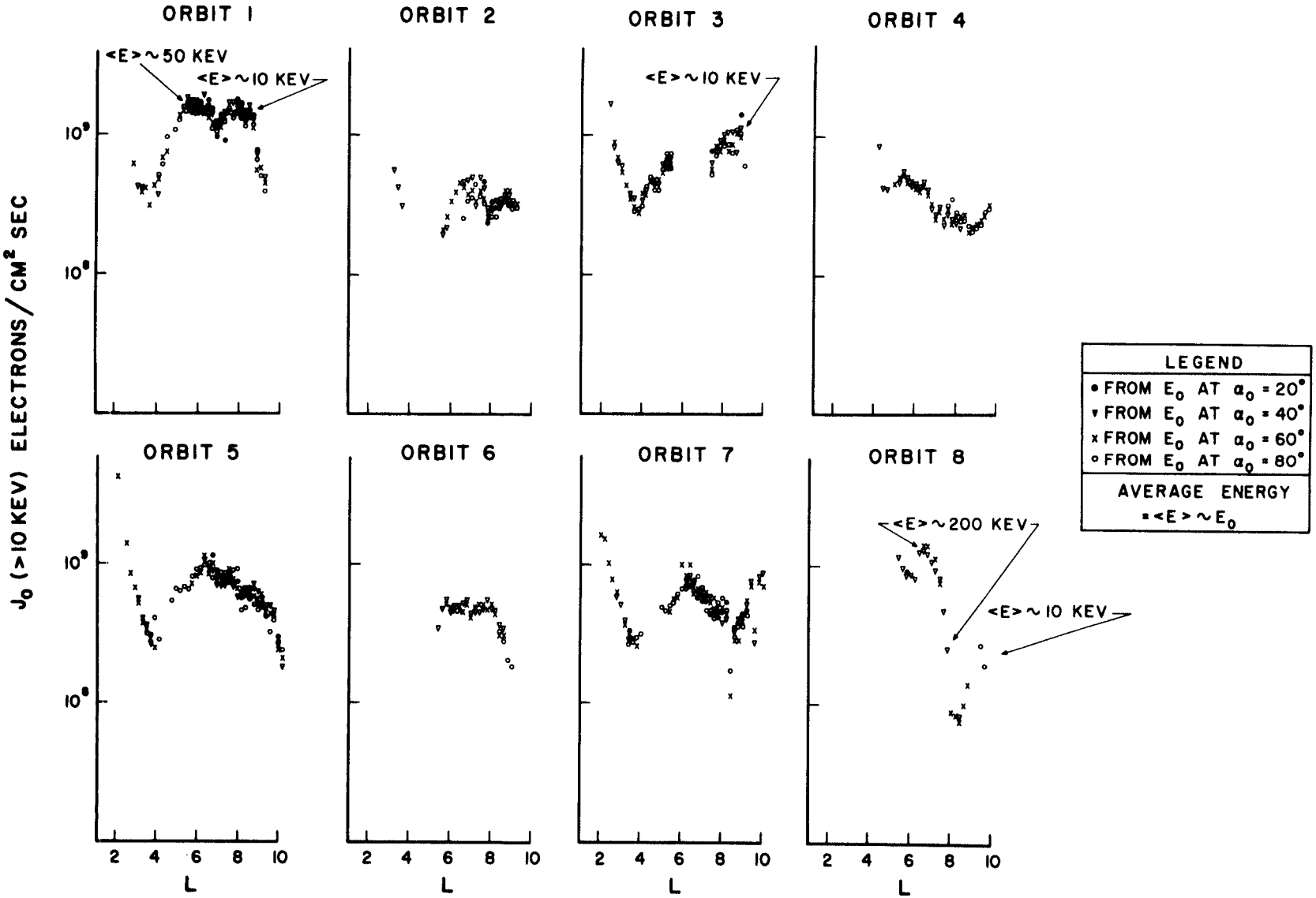
ORBIT 1
ORBIT 2
ORBIT 3
ORBIT 4
ORBIT 5
ORBIT 6
ORBIT 7
ORBIT 8
<E>~50 KEV
<E>~10 KEV
<E>~10 KEV
<E>~200 KEV
<E>~10 KEV
J_0 (>10 KEV) ELECTRONS / CM^2 SEC
10^9
10^8
2 4 6 8 10
L
LEGEND
• FROM E_0 AT $\alpha_0 = 20°$
▾ FROM E_0 AT $\alpha_0 = 40°$
× FROM E_0 AT $\alpha_0 = 60°$
○ FROM E_0 AT $\alpha_0 = 80°$
AVERAGE ENERGY
= <E> ~ E_0

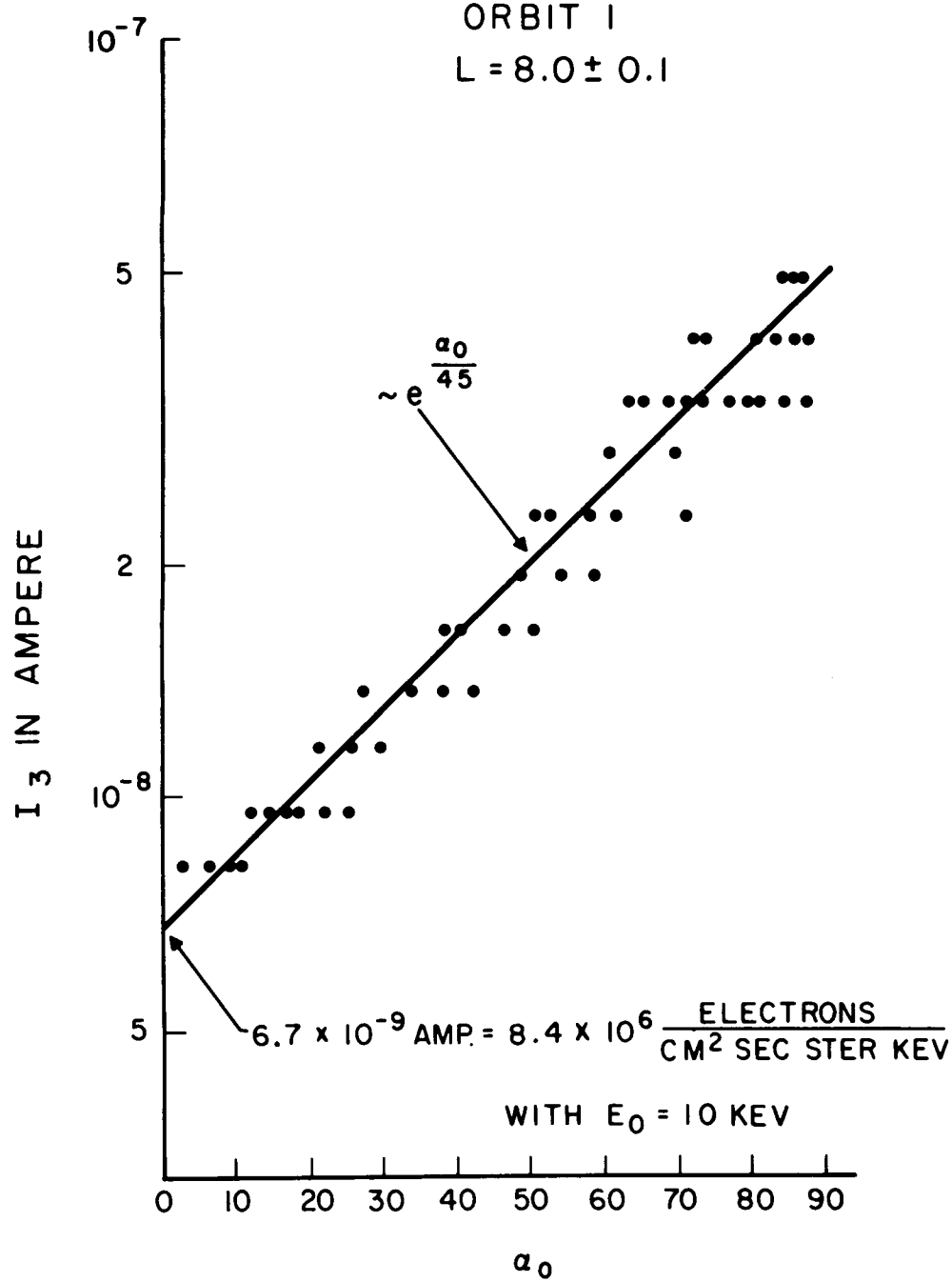
ORBIT I
L = 8.0 ± 0.1
10^{-7}
5
2
10^{-8}
5
I_3 IN AMPERE
$\sim e^{\frac{\alpha_0}{45}}$
6.7×10^{-9} AMP. = $8.4 \times 10^6 \frac{\text{ELECTRONS}}{\text{CM}^2 \text{ SEC STER KEV}}$
WITH E_0 = 10 KEV
0 10 20 30 40 50 60 70 80 90
α_0